JOURNAL OF SPACECRAFT AND ROCKETS
Vol. 31, No. 5, September–October 1994

Aerodynamic Characteristics of a Hypersonic Viscous Optimized Waverider at High Altitudes

Didier F. G. Rault*
NASA Langley Research Center, Hampton, Virginia 23681

The aerodynamic characteristics of a University of Maryland viscous optimized waverider are studied at altitudes ranging from 97 to 145 km and incidence angles of 0 to 30 deg. The direct simulation Monte Carlo method is used to simulate and analyze the flowfield around the waverider and evaluate surface loads. It is shown that the vehicle lift-to-drag ratio decreases rapidly as flight altitude is increased, and is confined to values less than 0.3. At high altitudes, the waverider is surrounded by a thick viscous shock layer, and the friction forces, which are typically large at high Knudsen numbers, are shown to significantly reduce lift and increase drag.

Nomenclature

C_L, C_D	= lift and drag coefficients
E	= energy flux
F_x, F_y, F_z	= force components in X, Y, Z directions
Kn	= Knudsen number
L	= characteristic length
L/D	= lift-to-drag ratio
$L_n = n/\nabla n$	= local gradient scale
M	= Mach number
n	= number density
P, p	= pressure force and pressure per unit area
S, s	= shear force and shear per unit area
V	= thermal velocity
V'	= rarefaction parameter
∇n	= density gradient magnitude
λ	= collision mean free path
ν	= nonequilibrium collision frequency
ω	= viscosity temperature exponent

Subscript

∞	= freestream

Introduction

HYPERSONIC waveriders have been shown to have the potential to generate high lift-to-drag ratios (L/D) at high Mach numbers. High lift is obtained by effectively using the shock as a valve to prevent airflow from the high pressure windside to the low pressure leeside. Waveriders were initially developed in the late 1950s by Nonweiler,[1] and extensive research has been devoted to them since that time. The full potential of waveriders, however, has never been fulfilled because of many factors, among which is the fact that viscous forces tend to displace the shock, and hence, degrade L/D ratios to well below their theoretical values. Recently, interest in waveriders has been renewed by the work done by the Hypersonic Group at the University of Maryland, wherein Anderson and his co-workers developed the so-called viscous optimized waverider.[2] The surface geometry of a viscous optimized waverider is generated through an iterative process in which pressure and skin friction forces are computed for a series of stream surfaces in a given generic flowfield (such as around a wedge or cone). The stream surface yielding the largest L/D ratio is then selected as the optimized body surface geometry.

Received Dec. 14, 1991; Presented as Paper 92-0306 at the AIAA 30th Aerospace Sciences Meeting, Reno, NV, Jan. 6–9, 1992; revision received Sept. 29, 1993; accepted for publication Oct. 6, 1993.

*Aerospace Technologist, Aerothermodynamics Branch, Space Systems Division. Member AIAA.

Hypersonic waveriders presently are being considered for high-altitude/low-density applications. Waveriders have been proposed to be used at the payload end of a tether to conduct fundamental aerothermodynamic research in the 90–150 km altitude range,[3] and more recently, waveriders have been considered for planetary and solar explorations, utilizing their high aerodynamic performance for efficient aerogravity-assisted maneuvering. In the high-altitude/high-Knudsen number flow regime, the shock and viscous layers are typically very thick and strongly interacting. The questions addressed in the present paper are the following: Is the basic concept of waveriding still applicable at high altitudes? How much do the large viscous forces degrade the aerodynamic performance of waveriders? The viscous optimized waverider is designed using a continuum flow methodology, and questions can be raised as to the suitability of such an approach in high-altitude applications.

The work presented in this paper is concerned with the high-altitude/high-Knudsen number aerodynamic performance of a specific viscous optimized waverider, with altitudes ranging from 97 to 145 km and Mach numbers around 25. At 90 km and above, the atmospheric air density is very low and the flowfield around a high altitude waverider would, therefore, be primarily in the transition and free molecular flow regimes, where viscous effects, shock-viscous interaction, velocity slip, and thermal nonequilibrium are important. The direct simulation Monte Carlo (DSMC) method of Bird,[4] was used in the present work.

This paper is in seven sections. In the first, the DSMC method is described, with special emphasis given to the particular features of the algorithm we use. The waverider surface geometry and test-flight conditions are described in the second. The waverider geometry was provided by Anderson et al.[5] The results of our simulation are presented and discussed in the third and fourth sections. Aerodynamic coefficients have been evaluated as a function of altitude and incidence angles. Our simulation yields lift-to-drag ratio values for high altitude viscous optimized waveriders that are much lower than those predicted by Anderson, Ferguson, and Lewis, who used a continuum approach corrected for rarefaction effects with a bridging formula.

In the fifth section, we compare the aerodynamic performance of a viscous optimized waverider with the performance of a delta wing with similar wetted surface area, base area, and length. It is shown that the viscous optimized waverider geometry yields a higher lift and a larger L/D ratio than a comparable delta wing.

The final two sections pertain to the simulation method itself. The sixth section describes the technique used to ensure that steady-state conditions had been reached in the simulation prior to initiating time averaging of microscopic samples. In the seventh section, a discussion on the effective surface area of bodies defined with our reduced resolution DSMC algorithm is presented. A method used to estimate the effective surface area is described. Details on the computation and simulation setup are compiled in an Appendix.

DSMC Method: Description of Present Algorithm

The DSMC algorithm used in the present study is the one developed for three-dimensional bodies by Bird[6] and incorporated into the F3 system of codes.[7] The F3 code is built around the same basic physical concepts as the more traditional DSMC codes.[4] A representative sample of gas molecules is selected and each simulated molecule is tracked in real time through intermolecular collisions, wall collisions, and translational motion. Intermolecular collisions (which are considered to be stochastic) and molecule translational motion (which is considered to be deterministic) are uncoupled in time and computed sequentially. The main difference between the F3 code and previous DSMC codes is in the definition of the spatial domain (computational grid) and the body surface.

The F3 computational grid is both Cartesian and unstructured. A uniform Cartesian mesh is uniquely suited for particle simulation; the tracking of simulated molecules and the assignment of each one to a grid cell requires a minimum number of arithmetic operations in a Cartesian grid. In contrast, tracking particles in a body-fitted grid requires somewhat lengthy three-dimensional computations of the intersection of particle trajectories with cell boundaries.[8]

A uniform grid, however, is not generally recommended in flow simulations, whether the flow regime is continuum or rarefied, because the computational grid spatial resolution must be tied to local gradient scales and/or mean free paths. These characteristic lengths vary markedly from relatively large values in the freestream to much lower values in the shock region and the near-body Knudsen layer. A uniform grid with a resolution based on the smallest length scale would lead to a very large number of small computational grid cells, which for three-dimensional particle simulation in turn would lead to an extremely large number of simulated molecules and high computer storage requirements, as shown by Feiereisen and McDonald.[9]

The computational grid we developed is shown in Fig. 1. Basically, it has two levels: a uniform background Cartesian mesh (BCM) (shown in the lower left corner), on which is superimposed the actual computational grid. A computational grid cell typically is made of several of the BCM parallelepiped cells and can have a somewhat arbitrary shape and aspect ratio. The BCM spatial resolution is a fraction of the freestream mean free path. Molecules are tracked in the BCM, and through a cross-reference array, assigned to their respective computational grid cells. In regions of large gradients or strong nonequilibrium, such as in the body vicinity or within a strong shock, a high resolution Cartesian mesh (HRCM) can be overlaid locally on top of the BCM (i.e., a BCM cell can be subdivided, and each subdivision is an HRCM cell). In these regions, computational grid cells are constructed on top of the HRCM (i.e., a computational grid cell is made of several of the HRCM cells), and molecules are tracked using both the BCM and the HRCM meshes.

This grid structure has several advantages. It exploits the main feature of Cartesian grids, namely, the high computational efficiency, while utilizing the main property of unstructured grids, namely, the flexibility to adjust the size of computational grid cells to local length scales (gradient scale and mean free path). This latter feature is used to adapt the computational grid in the course of a simulation to ensure optimal grid layout and appropriate positioning of the computational domain boundaries. The HRCM grid resolution is adjusted to the smallest collision mean free path near the body. For typical hypersonic problems, the use of this computational grid structure, as opposed to uniform Cartesian grid, leads to a decrease in the number of computational cells and simulated molecules by a factor of 20 (Refs. 9–11).

The surface of the simulated body is defined at the resolution of the HRCM mesh. In effect, the simulation code distorts the body surface so that the body conforms to the HRCM. To the naked eye, the body would, therefore, appear very granular, with the surface composed of building-block-like pixels, as illustrated in Fig. 2. To the molecules, however, the surface appears relatively smooth because the normal direction cosines of the original surface are also stored for each body surface element. The advantage of using such a coarse spatial representation of the body surface is twofold. First, the body surface geometry of even complex shaped three-dimensional vehicles can be stored as a relatively short list of integers (namely, the tag numbers of individual pixels containing a section of the body surface) and a corresponding list of direction cosines. Second, the gas/body surface interaction occurs only at the interface of Cartesian grid cells, which precludes the somewhat lengthy computations of the intersection of molecule trajectories with arbitrarily oriented planes. Some uncertainty as to the effective surface area of the body is introduced with this algorithm, as we describe later.

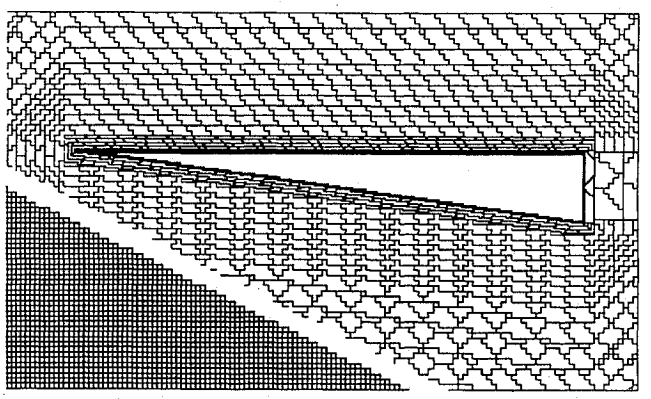

Fig. 1 Computational grid layout at 105 km in plane of symmetry. (See grid structure details in Ref. 6.)

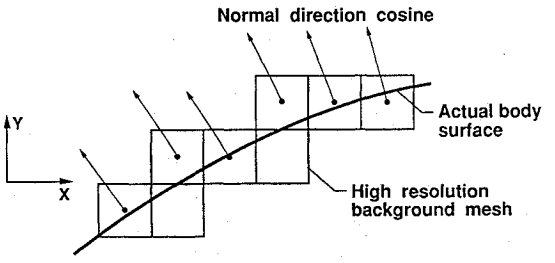

Fig. 2 Body surface definition.

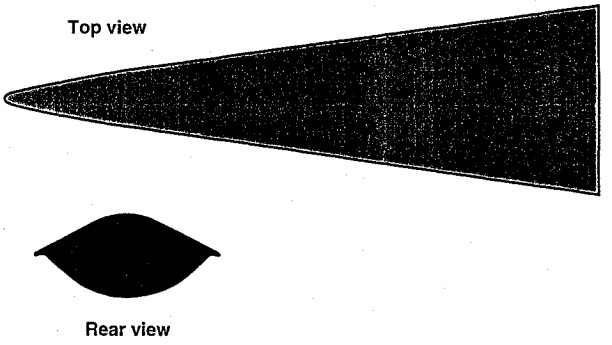

Fig. 3 Viscous optimized waverider geometry.

More detailed information on the F3 code can be found in Ref. 6 where Bird simulates the flowfield around a re-entering Space Shuttle Orbiter at altitudes ranging from 120 to 170 km, and Refs. 10 and 11, where Rault computes the aerodynamic properties of Delta wings at high Knudsen numbers.

Waverider Body Geometry and Simulation Test Conditions

Figure 3 shows the basic features of the waverider vehicle under study. The surface geometry was provided by Anderson et al.[5] as an X, Y, Z data file. This geometry had been optimized for a Mach number of 25, a nominal altitude of 90 km, and a ratio of specific heats of 1.4. The waverider geometry was generated using stream surfaces in the flowfield about a 7.6 deg cone. The vehicle is 5 m long with a base height of 0.654 m and a span of 1.536 m. The total wetted surface area is 9.9 m^2, including a base area of 0.59 m^2. The planform area is 4.236 m^2. In the optimization procedure, the waverider surface area was assumed isothermal at a temperature of 785 K.

Using the approach described in Ref. 6, Anderson has shown this body geometry to yield maximum L/D ratio at the nominal flight

Table 1 Simulated flight conditions (freestream gas density, temperature, and composition)

Nominal altitude, km	Number density, mol./m^3	Temperature, K	Gas composition N_2	O_2	O
97	$2.12\ 10^{+19}$	165	79	21	0
105	$5.02\ 10^{+18}$	225	78	15	7
115	$1.00\ 10^{+18}$	310	75	11	14
125	$3.00\ 10^{+17}$	435	72	7	21
135	$1.30\ 10^{+17}$	560	66	7	27
145	$6.90\ 10^{+16}$	670	63	6	31

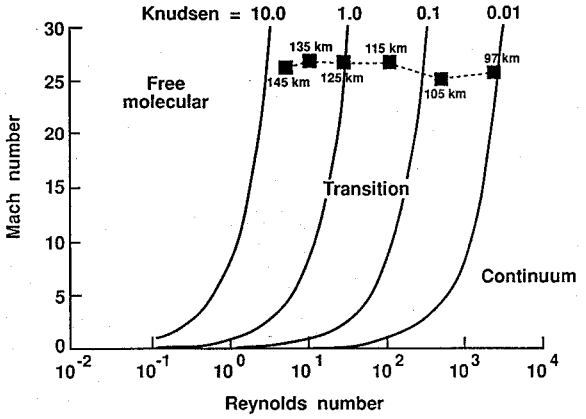

Fig. 4 Mach number–Reynolds number diagram.

conditions of 90 km altitude and Mach 25. The same body geometry has been used at all altitudes and incidence angles studied in the present work, although it is known not to yield the largest L/D ratio under these conditions.[6] This approach was used in this first study of viscous optimized waveriders at high Knudsen numbers explicitly to examine the effects of rarefied flow on the aerodynamic performance of waveriders and illustrate the major differences in flowfield structure and viscous shock-layer properties between the continuum and the rarefied flow regimes. The optimization scheme described in Ref. 6 is strictly applicable in that point of the continuum flow regime where shock/viscous interaction is weak, and as we will be shown, might not lead to the optimal design for high Knudsen number waveriders.

The flight conditions simulated in our computations are described in Table 1. The Mach numbers were held close to 25 at all altitudes. The test conditions are illustrated further in the Reynolds–Mach number diagram of Fig. 4 and in Table 2, where it can be observed that overall Knudsen numbers (based on waverider length and freestream density, temperature, and composition) vary from the near continuum value of 0.0106 to the near free molecular value of 5.57 as altitude increases from 97 to 145 km. As we show below, however, even at the smallest Knudsen number conditions, most of the flowfield around the waverider is in the transition flow regime. The local Knudsen numbers, based on density gradient scale and local mean free path, are almost always larger than 0.01.

The viscous interaction parameter[12] $\bar{\chi}$ is larger than 50 for all conditions studied, which means that, even at the least rarefied conditions, there is a strong interaction between the shock and the viscous layer.

Simulation Results

Figure 5 and Table 3 show values of the lift coefficient, C_L, drag coefficient, C_D, and lift-to-drag ratio L/D, as altitude is increased from 97 to 145 km. The aerodynamic coefficients are based on the planform surface area. In the present state of the F3 code, the simulation at 97 km required all the memory available on our workstation (64 Mbytes of 32 bit words), and simulations at lower altitudes were not done. In Fig. 5, open symbols represent the free molecular limit values corresponding to the freestream temperature and gas composition at a given altitude. As altitude is increased, the drag coefficient rapidly increases and reaches the free molecular limit value at about

Table 2 Simulated flight conditions (overall Reynolds, Mach, Knudsen numbers, based on vehicle length)

Nominal altitude, km	Reynolds	Mach	Kundsen
97	2630.0	25.4	0.0106
105	555.9	25.0	0.050
115	107.2	26.5	0.285
125	29.2	26.5	1.07
135	11.9	26.8	2.74
145	5.8	26.3	5.57

Table 3 Aerodynamic coefficients of a viscous optimized waverider as a function of altitude at 0-deg incidence

Altitude, km	C_L	C_D	L/D
97	$3.64\ 10^{-2}$	0.148	0.246
105	$4.65\ 10^{-2}$	0.236	0.197
115	$3.96\ 10^{-2}$	0.304	0.130
125	$2.89\ 10^{-2}$	0.339	$8.53\ 10^{-2}$
135	$2.06\ 10^{-2}$	0.347	$5.81\ 10^{-2}$
145	$1.54\ 10^{-2}$	0.329	$4.68\ 10^{-2}$

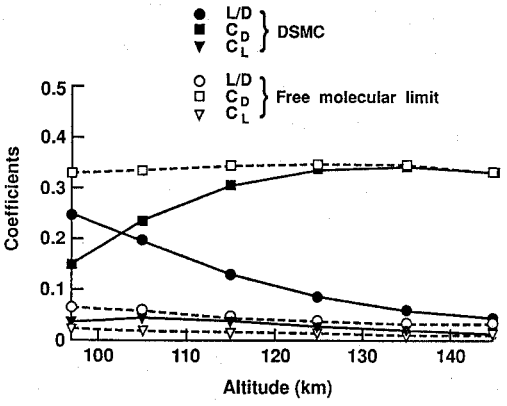

Fig. 5 Aerodynamic characteristics of viscous optimized waverider at 0-deg incidence.

130 km. The lift coefficient reaches a maximum value at 105 km, and then decreases toward its free molecular limit value. The L/D ratio monotonically decreases as altitude is increased. Upon extrapolating the computed values to lower altitudes, L/D ratio can be estimated to be about 0.3 at 90 km. This value is extremely low, much lower than the value of 1.4 estimated by Anderson,[12] but comparable with L/D values obtained by Kautz and Baron[13] and Galloway et al.[14] for caret type waveriders.

The free molecular limit shown in Fig. 5 varies as a function of altitude for two reasons. As altitude is increased, the atmospheric composition and temperature change, as shown in Table 1. Furthermore, these free molecular limits also contain information on the effective surface area of the waverider body. As described earlier, the waverider body is defined in the F3 code at a relatively coarse resolution, namely the resolution of the HRCM mesh. The resolutions of the two background meshes vary with altitude because, as altitude increases, density disturbances extend farther away from the body, and the computational volume necessarily increases, which leads to an effective stretching of the two background Cartesian meshes. This stretching of the background meshes reduces the resolution at which the body is being defined, which, in turn, leads to an increase of the effective surface area of the body.

Figure 6 and Table 4 show the value of the aerodynamic coefficients C_L, C_D, L/D, as incidence angle increases from 0 to 30 deg for a nominal altitude of 105 km. Figure 7 is a polar curve showing the drag coefficient as a function of the lift coefficient. A maximum lift-to-drag ratio of 0.320 can be observed to be reached at about 10 deg incidence. In the free molecular regime, shear stresses are significantly larger, and the maximum lift-to-drag ratio is 0.068 at 10 deg incidence.

Table 4 Aerodynamic coefficients of a viscous optimized waverider as a function of incidence angle at 105 km altitude

Incidence angle, deg	C_L	C_D	L/D
0	4.65 10^{-2}	0.236	0.197
10	0.128	0.400	0.320
20	0.201	0.646	0.312
30	0.261	0.930	0.281

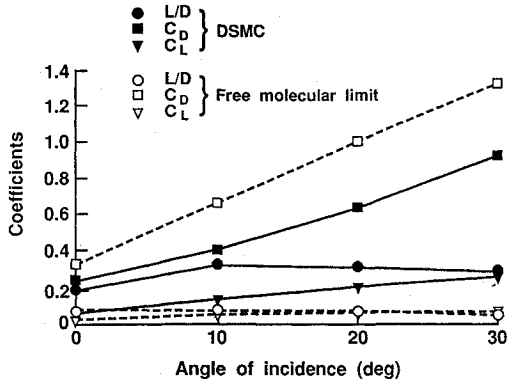

Fig. 6 Aerodynamic characteristics of viscous optimized waverider at 105 km.

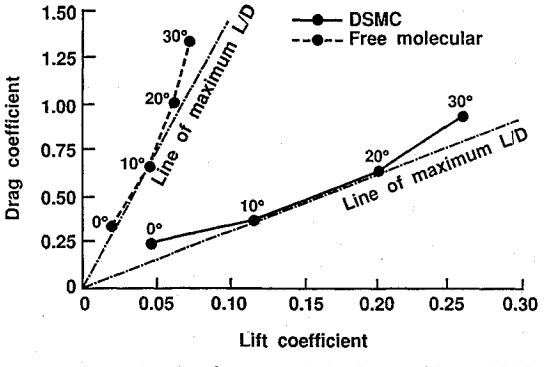

Fig. 7 Polar curve for the viscous optimized waverider at 105 km.

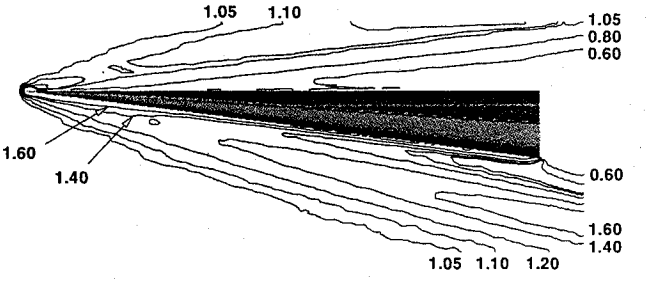

Fig. 8 Gas density n/n_∞ in the plane of symmetry of waverider at 97 km and 0-deg incidence.

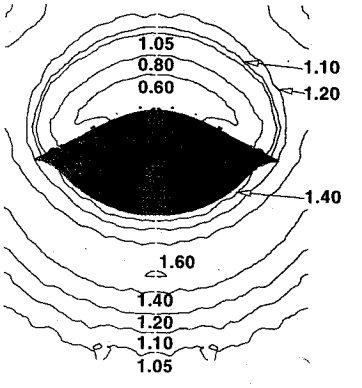

Fig. 9 Gas density n/n_∞ in the cross-section plane at 80% of the chord (altitude = 97 km, incidence = 0 deg).

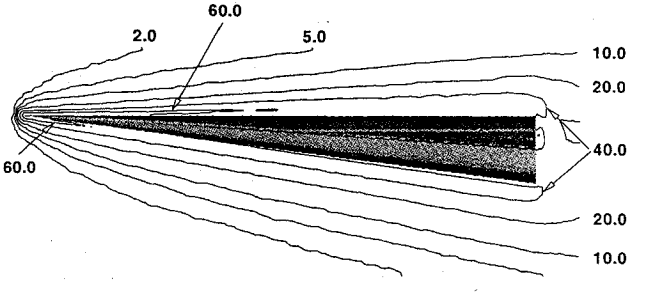

Fig. 10 Kinetic temperature (T/T_∞) in the plane of symmetry of waverider at 97 km and 0-deg incidence.

Figures 8 and 9 show the density field around the waverider at 97 km in the waverider plane of symmetry and in a cross-sectional plane at 80% of the chord. Densities are normalized to the freestream density, n_∞. The density contour maps are somewhat "noisy." The main emphasis in the present simulation was the computation of the aerodynamic forces on the waverider surface, and the simulation was interrupted once the aerodynamic coefficients had "converged" to stable values. A longer simulation would have resulted in larger molecular samples in each computational cell, and consequently, lower random noise. At 97 km, relatively weak shocks are created on both the windside and leeside, with density increases of 60% and 20%, respectively. On the windside, a high density layer is formed near the body surface, with a density increase of up to three times the freestream density. (This high density layer is extremely thin and is not visible in the figure.) A region of high kinetic temperature, and consequently low density, lies in between the shock front and the Knudsen layer. Figure 10 shows the kinetic temperature (as defined by Bird[4]), around the waverider at 97 km and 0 deg incidence angle.

Figures 11 and 12 show the magnitude of the density gradient around the waverider at 97 km and 0 deg incidence. These figures are similar to schlieren pictures, which are used in wind-tunnel data reduction to highlight regions of large density gradients, such as shocks and slip boundaries.[15] Schlieren techniques cannot be used in rarefied gas wind tunnels, because gas densities are too low to sufficiently refract light rays traversing the flowfield. A schlieren picture can, however, be generated from numerical data to highlight and identify the characteristic features of the simulated flowfield. From these figures, the following observations can be made. At the lower altitude, a fairly broad and diffuse shock can be observed on the waverider windside. This shock gradually weakens as altitude is increased. At higher altitudes, intermolecular collisions become very infrequent, and the flowfield has a shockless structure typical of free molecular flows. A high-density layer can be observed in the vicinity of the body. This wall layer and the shock are merged near the apex of the body and separate downstream. Figure 14 shows that the shock is not attached to the leading edge of the waverider; therefore, the waverider is not "riding on its shockwave," but rather on the viscous shock layer.

Figure 13 shows the value of the local Knudsen numbers around the waverider at 97 km and 0 deg incidence. For each cell of the computational grid, the local Knudsen number is evaluated as the ratio of the local mean free path to the local density gradient scale. The local mean free path is computed using the nonequilibrium value of the collision frequency ν, which is evaluated by storing the number of collisions suffered by a given species, namely oxygen molecules, in the course of the simulation. As can be seen in Fig. 13, although the waverider at 97 km has an overall Knudsen number of 0.0106, the flowfield around the waverider is mostly transitional.

Fig. 11a Density gradient magnitude in the plane of symmetry of waverider at 97 km altitude and 0-deg incidence.

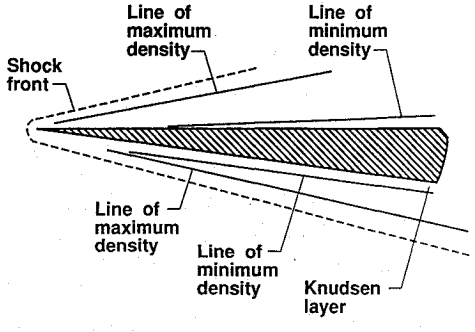

Fig. 11b Density gradient magnitude in plane of symmetry of waverider at 97 km and 0-deg incidence.

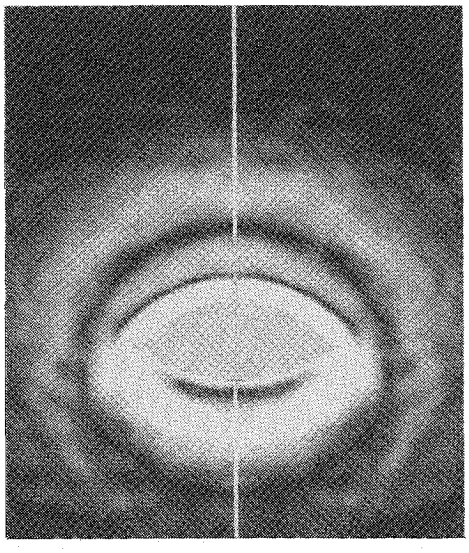

Fig. 12a Density gradient magnitude in the cross-section plane at 80% of the chord (altitude = 97 km, incidence = 0 deg).

Discussion of the Results

The lift-to-drag ratios of hypersonic optimized viscous waveriders are significantly lower in the transition and free molecular flow regimes (high altitudes, high Knudsen numbers) than they are in the continuum flow regime (low altitudes, low Knudsen numbers). The shear stresses (skin friction), which are typically large in rarefied flow regimes, are the main reason behind this performance degradation at high altitudes. As shown in Fig. 14, the shear stresses account for more than 93% of the drag forces on the waverider at 0 deg incidence angle above 97 km. Moreover, shear forces significantly reduce the lift forces as shown in Fig. 15. These combined effects lead to very low lift-to-drag ratios for waveriders at high altitudes. Figures 16 and 17 show the contribution of shear and pressure forces on the drag and lift coefficients at 105 km as the incidence angle varies from 0 to 30 deg. As the incidence angle is increased, the increase of lift pressure forces initially overcompensates the lift and drag degradation caused by shear, and the lift-to-drag ratio in-

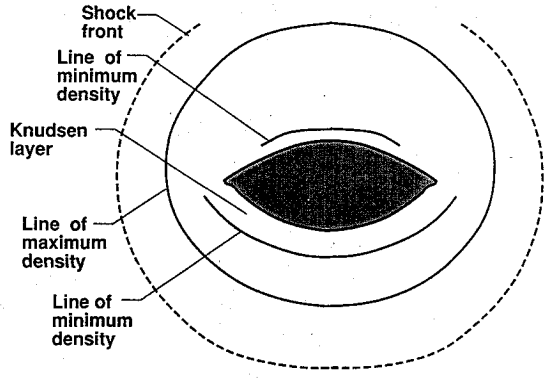

Fig. 12b Density gradient magnitude in cross-section plane at 80% of the chord (altitude = 97 km, incidence = 0 deg).

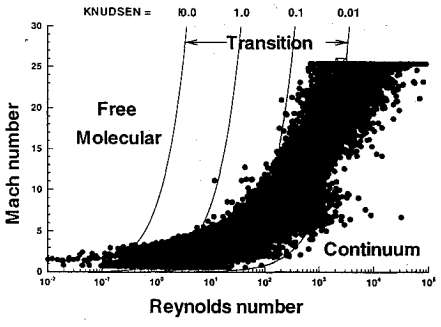

Fig. 13 Local Knudsen numbers for waverider at 97 km and 0 deg incidence.

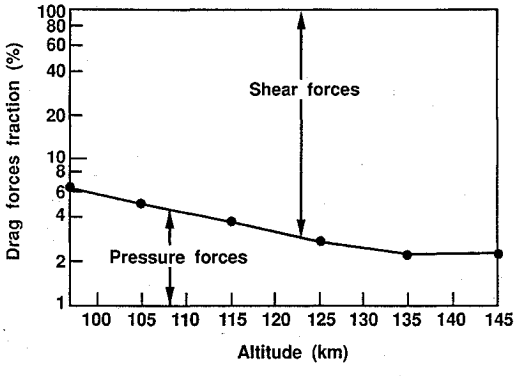

Fig. 14 Pressure and shear contribution to drag force on waverider at 0-deg incidence.

creases. At higher incidence angles, the shear forces and the drag pressure forces become very large, and the L/D ratio decreases. It can also be observed that, as incidence angle is increased, the pressure contribution to drag increases about twice as fast as the pressure contribution to lift.

The lift-to-drag ratios obtained in our present work are in the range of 0 to 1/3. Such values are too low to qualify the viscous

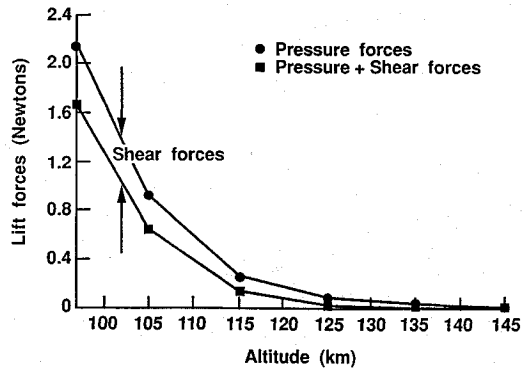

Fig. 15 Pressure and shear contribution to lift force on waverider at 0-deg incidence.

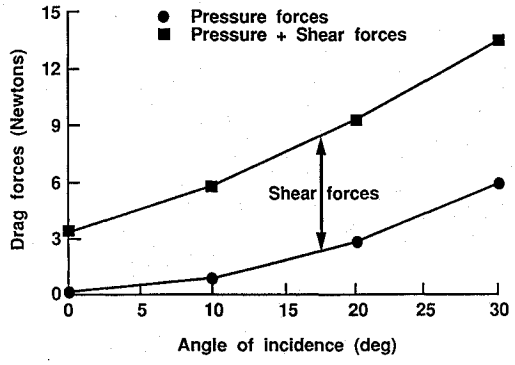

Fig. 16 Pressure and shear contribution to drag force on waverider at 105 km.

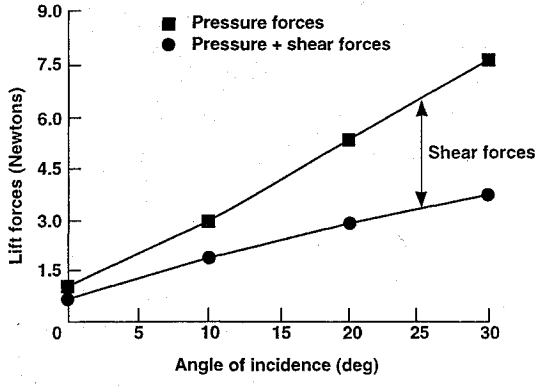

Fig. 17 Pressure and shear contribution to lift force on waverider at 105 km.

optimized waverider as a high L/D vehicle, and it would seem that this vehicle is not a viable candidate for missions requiring high lift-to-drag ratios at high altitudes. However, it must be remembered that the optimization procedure devised by Anderson is based on continuum flow methodology, assuming weak shock–viscous interaction. To design the vehicle geometry better for high-altitude applications (above 80 km), an optimization procedure based on transition and/or free molecular methodology should be devised, which would account for the unique features of high Knudsen flows, namely, thick shock, strong viscous effects, strong shock–viscous interaction, velocity slip, and temperature jump.

At a preliminary design stage of the optimization study, one could use the bridging formula established by Potter[16] to estimate the drag and lift coefficients of hypersonic bodies in the transition flow regime. The bridging formula is based on ground and flight experimental data, and relies on "the overriding importance of projected and wetted areas rather than details of body configuration."[16]

Figure 18 compares our present results with the ones evaluated with Potter's formula. The agreement is good between the DSMC

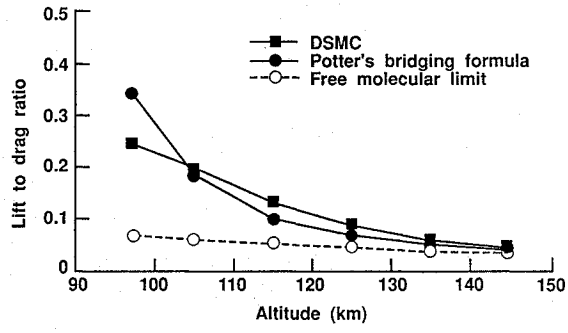

Fig. 18 Lift-to-drag ratio for waverider at 0-deg incidence. Comparison with Potter's bridging formula (Ref. 16).

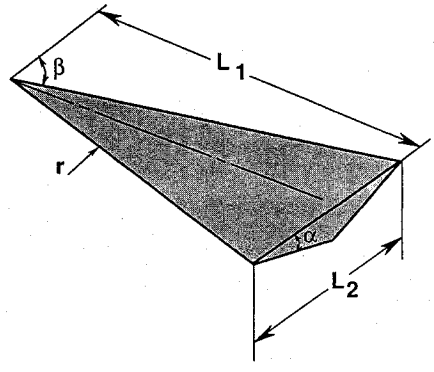

Fig. 19 Delta wing configuration.

and the bridging formula results at altitudes above 105 km, which would tend to show that aerodynamic performance at hypersonic speed and very low density, indeed, depends little on details of the body geometry, such as the small and sharp leading edges of the waverider wings (Fig. 3).

It is interesting to note that the independent parameters P_{n_D}, P_{n_L} in the bridging formula are, for large hypersonic Mach numbers, a direct function of the overall Knudsen number:

$$P_{n_D} = \left(\alpha\sqrt{K^*_{n_\infty}}/M_\infty^{\omega-0.5}\right) \tag{1}$$

where $K^*_{n_\infty}$ is the overall Knudsen number based on Potter's[16] characteristic length, M_∞ is the freestream Mach number, ω is the temperature coefficient of viscosity, and α is a constant. Similarly, Wilhite[17] has shown that in the near continuum and the strong interaction continuum regimes, the aerodynamic coefficients scale with the modified interaction parameter, $\bar{V}'$, which can be shown to be related to $\sqrt{K_{n_\infty}}$. Hence, it would seem that to the first order, the aerodynamic characteristics of a vehicle in the transition and near continuum flow regimes scale with the overall Knudsen number. Two waveriders having similar geometries, but different scales can, therefore, be expected to have the same aerodynamic characteristics if their overall Knudsen numbers are equal; for example, a 1 m waverider flying at 105 km would perform like a 5 m waverider flying at 115 km. (Atmospheric density decreases by a factor of 5 between 105 and 115 km.)

Performance Comparison: Viscous Optimized Waverider vs Delta Wing

The qualitative merit of the viscous optimized waverider geometry over other generic shapes can be ascertained by comparing its aerodynamic performance with the performance of bodies of different geometric shapes. A delta wing with comparable wetted surface area, base area, and length was studied for this purpose. Figure 19 and Table 5 show the main geometric characteristics of the delta wing. The flow around the delta wing was simulated for a Mach number of 25, an altitude of 97 km, and 0 deg incidence. Table 6 compares the computed aerodynamic coefficients and forces for the waverider and the delta wing. The shear forces

Table 5 Delta wing geometric characteristics

	Delta wing	Waverider
Length L_1, m	5.00	5.00
Span L_2, m	1.54	1.536
Leading-edge radius r, m	0.01	0.00
Base plane angle α, deg	45.00	——
Planform angle β, deg	81.20	——
Total wetted area, m^2	10.01	9.90
Base area, m^2	0.59	0.59
Planform reference area, m^2	3.85	4.236

Table 6 Aerodynamic performance comparison at 97 km, 0-deg incidence, waverider versus Delta wing

Aerodynamic forces, coefficients	Delta wing	Waverider
C_L	$3.07 \quad 10^{-2}$	$3.64 \quad 10^{-2}$
C_D	0.173	0.148
L/D	0.177	0.246
Pressure drag forces, N	0.429	0.435
Shear drag forces, N	6.837	6.392
Pressure lift forces, N	1.660	2.127
Shear lift forces, N	−0.375	−0.449

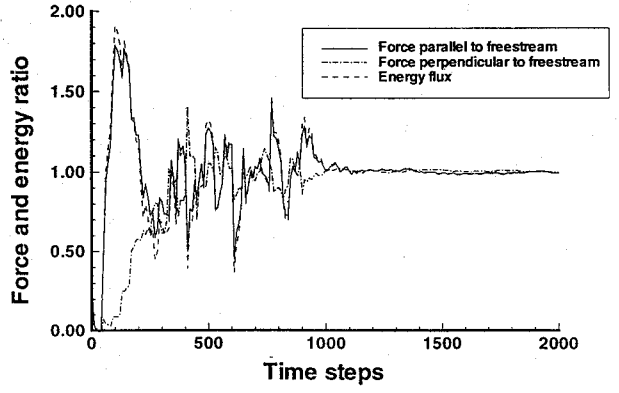

Fig. 20 Convergence time history for waverider at 105 km and 0-deg incidence.

in the longitudinal and transversal directions (i.e., parallel and perpendicular to freestream directions, respectively) can be observed to be similar for both models. This result was predictable because the wetted surface areas of both bodies are very close. The longitudinal pressure forces are also very similar, probably because both models have the same base surface area. However, the transversal pressure forces are different. The waverider generates somewhat larger transversal pressure forces, which yield larger lift and higher L/D ratio.

Steady-State Criteria for Aerodynamic Force Computation

In DSMC simulations, the values of aerodynamic forces typically "converge" rapidly, as compared with thermodynamic and flowfield properties, such as gas density and kinetic temperature. Whenever aerodynamic force evaluation is the prime objective in a simulation, such as in the present work, computational times can be significantly reduced if "convergence" criteria can be established that specifically apply to body surface forces. The criteria used in the present computation are as follows.

The aerodynamic forces acting on the vehicle can be computed in two different ways: 1) computing the momentum exchange each time a molecule hits the body surface; and 2) evaluating the net flux of momentum across the computational domain boundaries. At steady state, the two methods yield the same result, but in the transient phase of a simulation, these forces can be quite different. Figure 20 shows the ratios F_{x1}/F_{x2}, F_{y1}/F_{y2}, E_1/E_2 as a function of the number of simulation time steps, where F_{x1}, F_{x2} are the forces in the longitudinal X direction computed by the first and second methods, respectively; F_{y1}, F_{y2} are the forces in the transversal Y direction; and, E_1, E_2 are the molecule/wall energy exchange and the net energy flux across the computational domain boundaries.

Steady state is assumed, and microscopic sample time averaging is initiated, when each of these ratios has converged to unity. Confidence as to the accuracy of the force computed in this manner is gained by observing that the converged values contain information from both the body surface/molecule interaction simulation and the gas volume simulation.

Table 7 Effective wetted surface area of waverider[a]

Altitude, km	Incidence, deg	Effective surface area, m^2	HRCM spatial resolution, cm
97	0	10.28	0.96
105	0	10.66	1.59
115	0	11.63	2.74
125	0	12.40	3.51
135	0	12.83	3.53
145	0	10.71	1.84
105	10	10.07	1.63
105	20	10.24	1.63
105	30	10.60	1.63

[a]Actual wetted surface area of waverider = 9.90 m^2.

Effective Surface Area of a Body Defined at the F3 Code Resolution

As already described, the body surface in the F3 code is defined at a relatively low resolution. The body surface is specified as an ensemble of parallelepiped pixels, each pixel being a cell of the HRCM mesh. The effective surface area of the body, that is, the surface area "seen" by the molecules in the simulation, is therefore different from the actual surface area of the body. The value of the effective surface area is not known a priori. It lies in between the actual body surface area and the wetted surface area of the ensemble of body pixels. The fact that this latter bound is only an upper limit can be understood when considering the extreme limit of a zero temperature gas past a zero temperature body with a freestream velocity parallel to the X axis (see Fig. 2). For this limit case, the body pixel sides parallel to the freestream are not "seen" by the molecules, and the effective surface area of the body is not the total wetted area of the pixel assemble, but the surface area of all the pixel sides facing the freestream flow.

An estimate of the effective surface area of the body defined in the F3 code can be derived by considering the free molecular limit. The F3 code is first run in a mode where intermolecular collisions are "turned off," and the shear force S and pressure force P acting on each body surface element are computed and stored. Independently, using the free molecular theory, the forces-per-unit area, namely the shear s and pressure p, can be computed analytically for each body surface element using the normal direction cosine information stored for each body pixel. The effective surface area of each body surface element can then be derived as

$$A = S/s = P/p \tag{2}$$

The total effective area of the body is obtained by summing over all the surface elements on the body surface.

This technique for evaluating the effective surface area of a body defined by the F3 code is only strictly applicable to convex bodies at free molecular conditions. The waverider is primarily convex, with the exception being the little "winglets" shown in Fig. 3. This approach was used to estimate values of the effective surface area at all the altitudes considered in our simulation. Results are shown in Table 7 together with the spatial resolution considered in each case. As expected, the effective surface area increases as the spatial resolution decreases. For typical applications, this side effect of the reduced resolution scheme used in the F3 code should not impair the simulation results unduly. It must, however, be well understood and taken into account by the user during code preparation and code setup. In the present simulation, corrections of 10–20% should be applied to the aerodynamic coefficients computed at 115, 125, 135 km, and 0 deg incidence. If more exact results are desired, the spatial

resolution of the HRCM mesh would be increased to match effective and actual surface areas better.

Conclusions

The viscous optimized waverider studied in this paper at high Mach number/high Knudsen number conditions yields a relatively low lift-to-drag ratio. Shear forces, which are typically large in rarefied flow regimes, dramatically increase the drag and significantly decrease the lift. Moreover, the basic concept of a waverider, namely the principle of having a body "ride" on its own shock wave might not be applicable in rarefied flow regimes where, typically, viscous layers are very thick and shocks are broad, diffuse, and not attached to even razor sharp leading edges.

The concept of viscous optimization should be pursued to determine the optimal geometry of high-altitude hypersonic vehicles. Viscous optimization in this high Knudsen number domain should, however, be conducted with codes and numerical tools specifically designed for the rarefied flow regimes, instead of attempting to extend the use of continuum approach and methods to high Knudsen numbers. The contribution of shear stresses to the overall aerodynamic forces and the structure of the flowfield vary markedly as Knudsen number increases from continuum to free molecular values. As shown in this paper, three-dimensional DSMC simulation is now at a state where it can be used as an engineering tool and incorporated into an optimization design code.

Appendix

In this investigation, air is modeled as a nonreactive variable hard sphere gas with a viscosity temperature coefficient of 0.75. Air is assumed to be composed of three species, the properties of which are summarized in Table A1. Intermolecular energy transfer was modeled with the phenomenological model devised by Borgnakke and Larsen.[18]

The body is placed in the computational domain as shown in Fig. A1. It is rotated at the incidence angle with respect to the X axis, and the freestream is set parallel to the X axis. To capture the upstream shock structure and the near-wake expansion region, the upstream and downstream boundaries are positioned as shown in Table A2, which also shows the spatial resolution of the computational domain. The boundary conditions at each of the computational domain boundaries are specified as freestream inflow, except for the downstream boundary, which is assumed to be a vacuum interface, and the body plane of symmetry, which is assumed to be a specular reflection surface. Table A3 shows the time step, number of simulated molecules, and number of cells for each simulation case. The computational setup was checked a posteriori to give cell sizes smaller than local mean free paths and a time step smaller than the local residence time of a molecule within a cell. The bodysurface is assumed to be isothermal and fully diffuse for both momentum and energy.

The simulations described in this paper were performed on a Silicon Graphics IRIS workstation upgraded to a RAM memory of 64 Mbytes. Table A4 shows the CPU time and memory-requirements for each simulation case. Note that only the most CPU time memory-intensive test case (97 km at 0 deg incidence) was optimized. The other test cases could easily run within the hardware limitations of the workstation and no special effort was made to increase the code performance at these conditions.

Table A1 Characteristics of simulated air

	O_2	N_2	O
Molecular diam at 300 K, Angstroms	3.96	4.07	3.00
No. of rotational degrees of freedom	2	2	—
No. of collisions between rotational relaxation	5	5	—
No. of collisions between vibrational relaxation	50	50	—
Vibrational characteristic temperature, K	2270	3390	—

Table A3 Simulation setup

Altitude, km	Incidence, deg	Time step, μs	No. of cells	No. of molecules
97	0	1.46	41,000	$1.0\ 10^6$
105	0	2.06	8326	$4.0\ 10^5$
115	0	2.79	2648	$4.0\ 10^5$
125	0	2.95	4275	$3.0\ 10^5$
135	0	2.54	4732	$3.5\ 10^5$
145	0	1.21	4301	$4.0\ 10^5$
105	10	2.11	10,339	$4.0\ 10^5$
105	20	2.11	13,455	$4.5\ 10^5$
105	30	2.11	13,458	$7.0\ 10^5$

Table A4 Code performance on Silicon Graphics IRIS 4D/340 (single CPU, single precision)

Altitude, km	Incidence, deg	Total CPU time, h	Memory, Mbytes
97	0	18	60
105	0	6	36
115	0	7	37
125	0	6	22
135	0	7	30
145	0	11	49
105	10	6	32
105	20	7	42
105	30	8	46

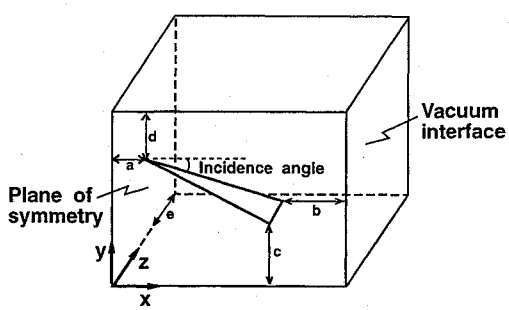

Fig. A1 Simulation computational domain.

Table A2 Simulation setup

		Offsets, m (Fig. A1)						
Altitude, km	Incidence, deg	a	b	c	d	e	BCM resolution	HRCM resolution
97	0	0.60	0.30	0.90	0.60	0.18	209 × 77 × 33	3 × 3 × 3
105	0	0.77	0.51	1.54	1.28	0.51	132 × 73 × 27	3 × 3 × 3
115	0	2.60	1.28	3.96	3.86	1.29	111 × 105 × 25	3 × 3 × 3
125	0	2.51	0.71	4.28	4.28	1.43	78 × 88 × 21	3 × 3 × 3
135	0	3.29	1.00	4.94	3.95	2.19	89 × 92 × 28	3 × 3 × 3
145	0	4.68	0.94	5.35	3.41	2.08	116 × 103 × 31	5 × 5 × 5
105	10	0.51	0.26	1.80	1.00	0.26	119 × 91 × 21	3 × 3 × 3
105	20	1.00	0.26	2.30	1.00	0.26	126 × 119 × 21	3 × 3 × 3
105	30	1.00	0.26	2.30	1.00	0.26	118 × 135 × 21	3 × 3 × 3

References

[1]Nonweiler, T. R., "Aerodynamic Problems of Manned Space Vehicles," *Journal of the Royal Aeronautical Society*, Vol. 63, 1959, pp. 521–528.

[2]Bowcutt, K. G., Anderson, J. D., and Capriotti, D. P., "Viscous Optimized Hypersonic Waveriders," AIAA Paper 87-0272, Jan. 1987.

[3]Anderson, J. L., "Tethered Aerothermodynamic Research for Hypersonic Waveriders," *Proceedings of First International Hypersonic Waverider Symposium*, Univ. of Maryland, College Park, MD, Oct. 1990.

[4]Bird, G. A., *Molecular Gas Dynamics*, Clarendon Press, Oxford, England, UK, 1976.

[5]Anderson, J. D., Ferguson, F., and Lewis, M. J., "Hypersonic Waveriders for High Altitude Applications," AIAA Paper 91-0530, Jan. 1991.

[6]Bird, G. A., "Application of the Direct Simulation Monte Carlo Method to the Full Shuttle Geometry," AIAA Paper 90-1962, June 1990.

[7]Bird, G. A., *The F3 Program System User's Manual*, G.A.B Consulting, June 1990.

[8]Celenligil, M. C., and Moss, J. N., "Application of the DSMC Method to Hypersonic Flow about a Delta Wing," *Seventeenth International Symposium on Rarefied Gas Dynamics* (Aachen, Germany), July 1990, pp. 778–783.

[9]Feiereisen, W. J., and McDonald, J. D., "Three Dimensional Discrete Particle Simulation of an AOTV," AIAA Paper 89-1711, June 1989.

[10]Rault, D. F. G., "Aerodynamic Performance of Delta Wings in the Hypersonic Rarefied Flow Regime," Workshop on Hypersonic Flows for Reentry Problems," Antibes, France, April 1991.

[11]Rault, D. F. G., "An Efficient DSMC Algorithm Applied to a Delta Wing," AIAA Paper 91-1316, June 1991.

[12]Anderson, J. D., *Hypersonic and High Temperature Gas Dynamics*, McGraw Hill, New York, 1989.

[13]Kautz, F. A., II, and Baron, J. R., "Direct Simulation of Waveriders in Hypersonic Rarefied Flow," AIAA Paper 91-1317, June 1991.

[14]Galloway, E. M., Gilmore, H. R., Harvey, J. K., and Jefferey, R. W., "Heat Transfer to a Delta Wing and Two Waverider Wings in a Rarefied Hypersonic Flows," *Proceedings of the First International Hypersonic Waverider Symposium*, Univ. of Maryland, College Park, MD, Oct. 1990.

[15]Liepmann, H. W., and Roshko, A., *Elements of Gasdynamics*, Wiley, New York, 1957.

[16]Potter, L. J., "Procedure for Estimating Aerodynamics for Three-Dimensional Bodies in Transitional Flow," *Rarefied Gas Dynamics: Theoretical and Computational Techniques*, edited by E. P. Muntz, D. P. Weaver, and D. H. Camp, Progress in Astronautics and Aeronautics, Vol. 118, AIAA, Washington, DC, 1988, pp. 484–492.

[17]Wilhite, A. W., Arrington, J. P., and McCandless, R. S., "Performance Aerodynamics of Aero-Assisted Orbital Transfer Vehicles," AIAA Paper 84-0406, Jan. 1984.

[18]Borgnakke, C. and Larsen, P. S., "Statistical Collision Model for Monte, Carlo Simulations of Gas Mixtures," *Journal of Computational Physics*, Vol. 18, 1975.